Correlative spectroscopic investigations of the mechanisms of inhomogeneity in CVD-grown monolayer WS$_2$

Liqin Su[1,2], Yifei Yu[3], Linyou Cao[3] and Yong Zhang[2*]

ABSTRACT Chemical vapor deposition (CVD) has been proved to be the most useful method to produce two-dimensional (2D) materials, including tungsten disulfide (WS$_2$). However, the existence of inhomogeneity of strain, doping, and defects in the CVD-grown WS$_2$ monolayers may significantly influence the optical and electronic properties of the materials, thus affecting their device applications. In this work, we systematically characterized the inhomogeneity of strain, doping, and nonradiative defect centers in mesoscopic-size, triangular-shape monolayer WS$_2$ grown by CVD on sapphire substrate by using spatially resolved micro-Raman and photoluminescence (PL) spectroscopy. We performed correlative analyses on the variations of the pertinent spectral parameters (i.e., peak position, intensity, and full width at half maximum) of Raman and PL signatures in two physical scales: (1) the complete-data-set level, including the data of the whole sample, and (2) the sub-data-set level for individual special regions (e.g., apexes, edges, center) that exhibit distinctly different strain, doping, and defect states. This study reveals and explains the inhomogeneous strain, doping, and defects across the WS$_2$ monolayer. Additionally, we find the inhomogeneity substantially diminishes when a mesoscopic-size triangle structure expands into a continuous film. Our work demonstrates that the correlative analyses, supported with physics insights, can offer comprehensive understanding on the underlying mechanisms of the inhomogeneity and guidance for optimizing the growth process and device processing of 2D materials.

Keywords: tungsten disulfide, Raman spectroscopy, photoluminescence, chemical vapor deposition

INTRODUCTION

Few-monolayer transition metal dichalcogenides (TMDs) have attracted tremendous interest in recent years due to their interesting electronic and optical properties [1–3]. Unlike graphene intrinsically with zero bandgap [4], monolayer semiconducting TMDs, such as MoS$_2$, MoSe$_2$, WS$_2$ and WSe$_2$, have direct bandgaps covering the visible to near-infrared spectral range, offering great potentials in practical applications such as light-emitting diodes (LEDs) [5], field-effect transistors (FET) [6], photodetectors [7], and solar cells [8]. High-quality monolayer TMDs can be produced by mechanical exfoliation and liquid-phase exfoliation [9], but these approaches are only suitable for the purpose of small-scale research. In contrast, chemical vapor deposition (CVD) has been proved to be a more practical methodology to produce large-scale TMD monolayers suitable for the realistic device applications [10]. Besides the difference in size, transferred and epitaxially grown materials may exhibit rather different properties [11,12]. Some differences are intrinsic in nature. For instance, the film-substrate bonding and thus charge exchange between the transferred and epitaxial film [11,12], even the epitaxial films on different substrate types [12–14] can be rather different; other differences are related to extrinsic factors, such as contaminations, imperfect transfer to other substrates, and growth inhomogeneity. Some inhomogeneities (e.g., wrinkles and bubbles) are inevitable for a transferred film as a result of imperfect contact with the supporting substrate [15], and thus the epitaxial film is expected to be more uniform. Most previous studies appear to emphasize the generic differences between the epitaxial techniques (e.g., different substrates [14]). In fact, even for the same substrate type, the properties of CVD-grown TMD materials are very sensitive to the growth conditions, such as the substrate condition, temperature, gas flow rate, and precursors [16–18], just like the growth of any other materials. Furthermore, depending on the substrate condition and growth mechanism, a single epitaxial TMD film might exhibit significant spatial inhomogeneity in the film morphology, crystalline domain structure, impurities and defects, which is particularly critical for fabricating micro/nanoscale devices as well as fundamental understanding of the material. Therefore, it is of immense importance to understand the effects and underlying mechanisms of the inhomogeneity, which could shed light on improving the crystalline quality and tuning the properties of the monolayer TMDs.

It has been well documented that the direct-bandgap nature of a monolayer TMD enables a strong light emission corresponding to the band-edge excitonic transition, normally marked as X$_A$ exciton in the literature [19,20]. In addition to the neutral excitons, charged excitons, so called trions, may also form when free charges are present. The trion transition often dominates the photoluminescence (PL) spectrum, labeled as X$_A-$ for the electron-bound exciton and X$_A+$ for the hole-bound exciton [20]. Quite a few studies have reported that both neutral and charged excitons are sensitive to doping and strain [21,22]. The doping can induce various structural defects introduced in the growth process, including point defects, dislocations, grain

[1] College of Optical and Electronic Technology, China Jiliang University, Hangzhou 310018, China
[2] Department of Electrical and Computer Engineering, The University of North Carolina at Charlotte, Charlotte, NC 28223, USA
[3] Department of Materials Science and Engineering, North Carolina State University, Raleigh, NC 27695, USA
* Corresponding author (email: yong.zhang@uncc.edu)

boundaries, edges, and substrates [23,24]. In most CVD-grown TMD monolayers, the X_A- trions rather than X_A+ emerge because of the native n-type doping, and the increase in the electron carrier concentration enhances X_A- emission in the PL spectrum [20]. The strain that originates from the thermal expansion coefficient (TEC) difference and lattice mismatch between the substrate and the TMD monolayer may also modify the optical properties of the material. For example, the epitaxial tensile strain could induce redshifts in PL peak and Raman mode frequencies [12,22]. In fact, both doping and strain effects in most cases coexist in the CVD-grown film and are often non-uniform across the material. Besides the doping and strain effects, deep trap states also play important roles in determining the (opto)electronic properties of the monolayer TMDs [25].

Despite a large volume of reports on monolayer TMDs, the inhomogeneity of strain and doping effects in CVD-grown TMD monolayers has only been examined briefly in the literature with little in-depth investigation of the mechanisms [7,26,27], let alone the non-uniformly distributed deep-state defects introduced during the growth. In this work, we focus on the CVD-grown monolayer WS_2 in one specific shape, i.e., triangular, which is perhaps the most commonly observed shape for a small size (of the order of tens of microns) epitaxial film. The variations of strain, doping, as well as deep defects across the as-grown WS_2 monolayer films will be investigated with two spatially resolved and mutually correlated spectroscopy techniques: Raman and PL spectroscopy. The results of both techniques are sensitive to strain, doping, and defects, which can provide information for the underlying mechanisms to better understand the growth process. By combining spatially resolved PL and Raman techniques, we examine not only the correlations in peak position, intensity and linewidth between PL and Raman data from the entire triangular sample but also the correlations for individual special regions (e.g., apexes, edges, and center) on the triangular film that exhibit distinctly different strain, doping, and defect states. The two-level correlation analysis, on both global and regional scales, is more revealing, because different mechanisms may be responsible for the same spectroscopic change in different samples or locations. For instance, low PL intensities in two samples or locations, A and B, might be due to two very different mechanisms: nonradiative recombination in A and doping in B. With this two-level correlation analysis and the help of physical insights, for the first time, we are able to disentangle the complexity of the three dominant mechanisms (strain, doping, and defects) that contribute to the inhomogeneity in CVD-grown TMD monolayers.

RESULTS AND DISCUSSION

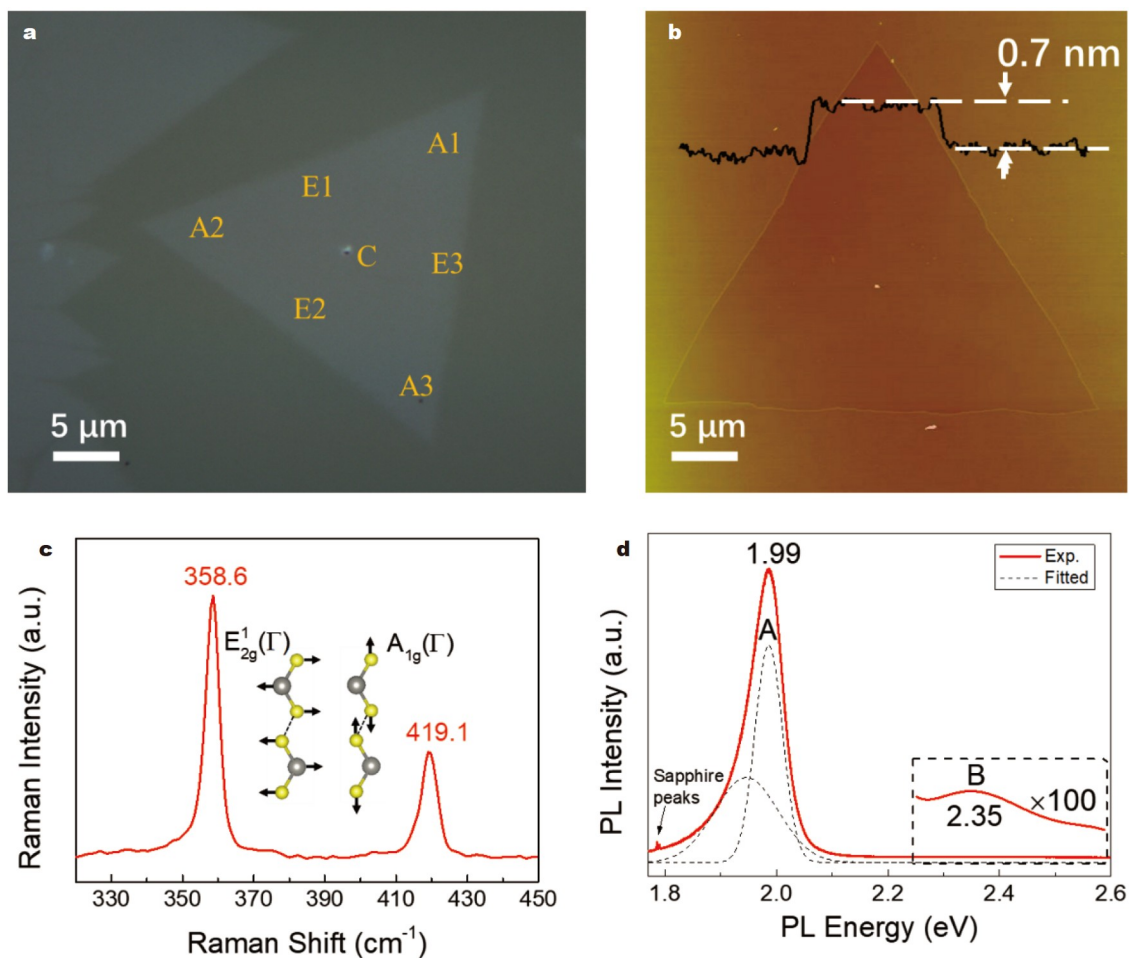### Growth and characterizations of monolayer WS_2

WS_2 monolayers were synthesized on sapphire by CVD with the sulfurization of WO_3 precursors at a temperature of 900°C, involving the expanding and thinning of WS_{2+x} flakes and eventually forming large monolayer WS_2 triangles (in the order of 10 μm in size) [28]. One can envision that the sulfurization process may vary dramatically within the monolayer triangle, because the growth time is longer near the center than that along the edge. Therefore, the composition deviation x could be either positive or negative, varying from one region to another. In addition, the interfacial interaction such as the chemical bonding between the film and substrate may also be spatially dependent.

The spatial variations in both composition and interfacial bonding in turn cause inhomogeneous strain, doping, and defect distributions over the triangle. It is important to investigate such triangle structures because on the one hand, they can be directly used for processing devices with a bottom-up approach, and on the other hand, they are the precursors to form a continuous film. In this work, μ-Raman and PL measurements were performed with a Horiba LabRAM HR800 system using a 441.6-nm excitation laser with a 100× lens (NA = 0.9), and the spectral resolution was better than 1 cm^{-1}. The reason to use 441.6-nm excitation was to avoid the resonance Raman effect, caused by the X_B exciton located at ~2.35 eV, which may complicate the analysis [12]. Note that all the data were obtained right after the growth of samples, and the oxidation of the WS_2 film is expected to be negligible [29].

Fig. 1a shows an optical image of an as-grown WS_2 triangle film on sapphire with an atomic force microscopy (AFM) image shown in Fig. 1b, indicating the thickness of the WS_2 monolayer is ~0.7 nm. For ease of reference, the different regions of the triangle in Fig. 1a are classified into three categories: (1) apex regions, as A1, A2, and A3, (2) edge regions, as E1, E2, and E3, and (3) central region, as C. Fig. 1c, d depict typical room-temperature (RT) Raman and PL spectra acquired from the region C with a laser power of ~120 μW. It is well known that the layer number of TMDs can be determined by means of Raman spectroscopy [30]. The frequency difference between two major Raman modes, in-plain mode (E_{2g}^1) and out-of-plane mode (A_{1g}), increases monotonically with the layer number. The frequency difference between E_{2g}^1 and A_{1g} is measured to be 60.5 cm^{-1}, indicating the film is monolayer [30]. For PL, a pronounced asymmetric lineshape with its peak at around ~1.99 eV is observed. The PL spectrum is fitted with a Gaussian lineshape function, and deconvoluted into two peaks with the energies of 1.99 and 1.95 eV, respectively. The higher-energy peak can be assigned to the X_A exciton emission, while the lower-energy peak is ascribed to the X_A- trion emission. The trion binding energy is estimated to be ~40 meV, which is consistent with the literature values [31]. A weak B exciton emission is also visible at ~2.35 eV.

Inhomogeneity of Raman and PL mapping

It is known that Raman spectrum of monolayer TMDs, including WS_2, can be significantly affected by strain and doping but in distinctly different ways. Under tensile strain, both E_{2g}^1 and A_{1g} modes are expected to redshift in their peak positions, but A_{1g} mode is less sensitive to strain than E_{2g}^1 mode [22,32]. In contrast, due to the symmetry of conduction band edge state in the monolayer WS_2, the stronger electron-phonon coupling makes A_{1g} mode more sensitive to the doping concentration than E_{2g}^1 mode, which results in more redshift or mode softening of A_{1g} mode [33,34]. Therefore, qualitatively, the shift of E_{2g}^1 mode can be used to describe the strain distribution across the WS_2 film, while A_{1g} mode is to be adopted to analyze the inhomogeneity of doping in the material. Similarly, PL lineshape is susceptible to strain and doping effects as well, whereas PL intensity is sensitive to the level of nonradiative recombination centers induced by the defects. It has been reported that the PL peak position redshifts when the in-plane tensile strain is applied to the film, while the doping may also lead to the redshift in the PL peak energy, but the effect only becomes appreciable when a relatively high doping concentration is present in the film

Figure 1 Characterizations of the CVD-grown monolayer WS_2. (a) Optical image and (b) AFM image of a WS_2 triangle on sapphire substrate, respectively. (c) Representative Raman and (d) PL spectra acquired from the central region of a triangle.

[35,36]. However, the increasing of the doping level normally broadens the full width at half maximum (FWHM) of the PL spectrum. Therefore, the peak energy of PL spectrum is a valid indicator of strain, the FWHM can be utilized to probe the doping concentration variation across the film, and the PL intensity reflects the level of nonradiative recombination centers.

Correlations of the Raman and PL mapping results

Fig. 2 presents high spatial resolution Raman and PL mapping results of the WS_2 triangle shown in Fig. 1a. In general, the central region, except for the very center (likely the nucleation site), appears to be more uniform for all spectroscopy parameters probed, whereas the edge and apex regions show more variations. We first analyzed the peak positions. Apparently both peak position and intensity of Raman modes and band-edge PL exhibit inhomogeneity across the triangle. Similar inhomogeneity is also observed in other triangles from the same growth procedure (Fig. S1). For the Raman mode peak positions, qualitatively, the map of the E_{2g}^1 mode shown in Fig. 2a shares some similarity with that of the A_{1g} mode of Fig. 2b: the E3 region shows redshifts relative to other regions or the spatially averaged value, which is in stark contrast with the E1 and E2 regions that instead show overall blueshifts. However, there are some subtle differences between the two modes: A_{1g} exhibits redshifts in A1

and A2, while in the central region (C), E_{2g}^1 shows slight redshifts and A_{1g} blueshifts. The PL peak position map in Fig. 2c exhibits the similar dominant patterns as those of E_{2g}^1 and A_{1g} showing blueshifts in the E1 and E2 regions and redshift in E3. These characteristics are likely related to the strain and doping that were introduced during the growth process.

Strain is the most straightforward cause of the shifts of the Raman and PL peaks. The strain is introduced to the film due to the TEC difference between the sapphire and WS_2 [12,37,38], during the final fast-cooling stage of the growth process [28]. However, the strain is likely inhomogeneous in the film. First, we assume that strain is the only factor for the shifts of Raman and PL peak positions. In order to quantitatively estimate the variations of the growth-induced strain in the triangle from the Raman and PL peak positions, we extracted the strain variations based on the density-functional theory calculations reported previously [12]. The deformation potentials for uniform strain are -4.4 cm^{-1}/%, -1.7 cm^{-1}/%, and -140 meV/% for the E_{2g}^1 and A_{1g} mode, and band gap E_g, respectively. The maximum E_{2g}^1 frequency difference over the triangle is estimated to be 3.26 cm^{-1}, and the corresponding strain difference is 0.74%. For the A_{1g} mode and PL peak positions, the corresponding maximum differences are 2.24 cm^{-1} or 1.32% and 86.8 meV or 0.62%, respectively. Since the maximum strain differences
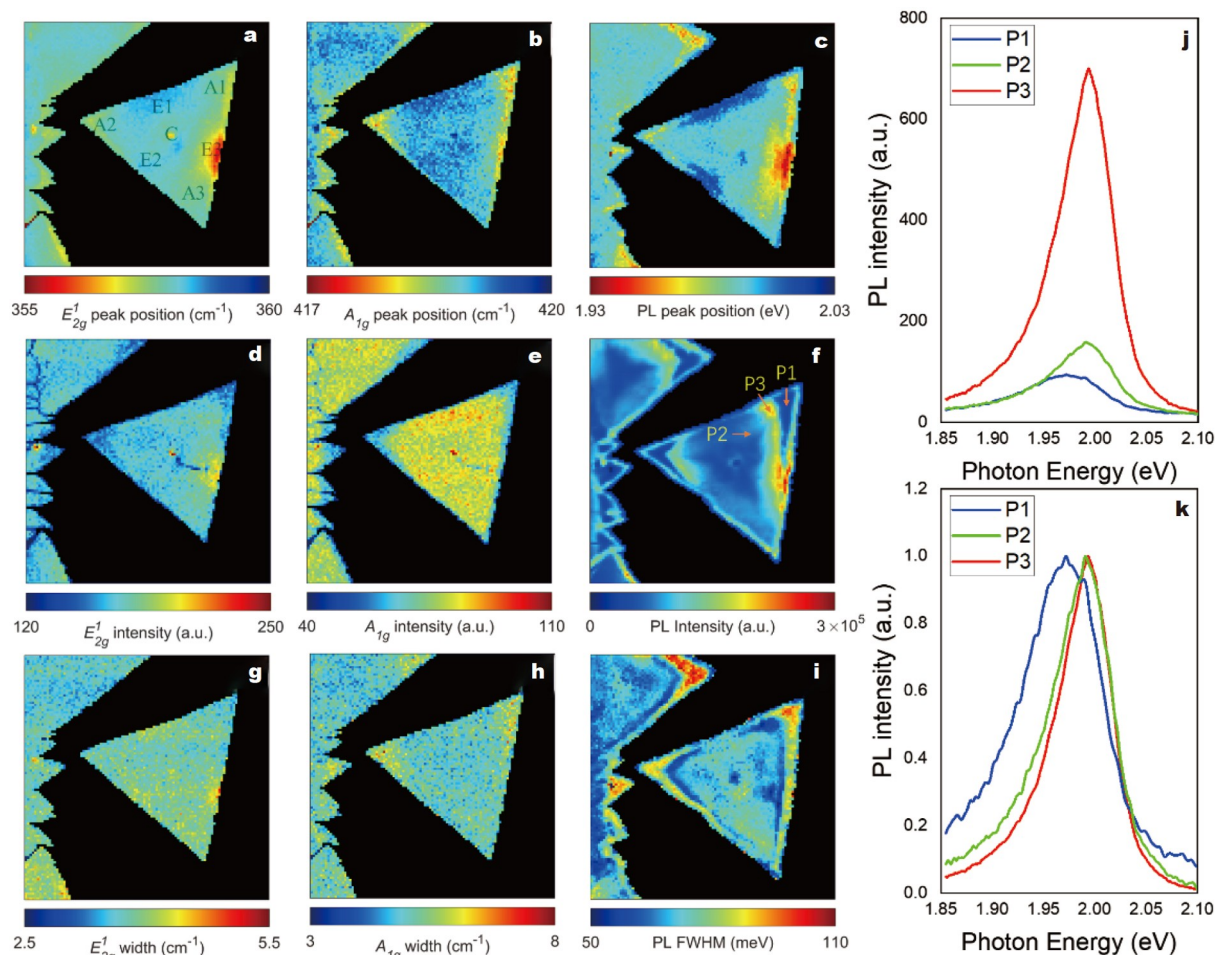
Figure 2 Raman and PL mappings of the monolayer WS$_2$ (50 μm × 50 μm). (a–c) Peak position maps, (d–f) intensity maps, and (g–i) FWHM maps of the E$_{2g}^1$ mode, A$_{1g}$ mode, and PL, respectively. (j) Representative PL spectra collected from P1, P2 and P3 locations. (k) Normalized PL spectra of (j).

extracted from the peak position maps of the E$_{2g}^1$ and A$_{1g}$ modes and PL are not necessary from the same measured locations, we carried out a statistic analysis of the strain difference between the edge and apex regions by subtracting the mean peak position of the edge regions (E1, E2, and E3) from that of the apex regions (A1, A2 and A3). The average frequency/photon energy difference between the edge and apex regions for the E$_{2g}^1$ mode is estimated to be 0.18 cm^{-1}, with that of A$_{1g}$ mode of 0.36 cm^{-1}, and that of PL of 6.2 meV, which corresponds to strain differences of 0.045%, 0.21% and 0.041%, respectively. In both analyses, the strain differences extracted from the E$_{2g}^1$ mode match quite well with those from PL. However, the abnormally large values of strain differences extracted from the A$_{1g}$ mode imply that the strain might not be the only mechanism for the inhomogeneity.

Fig. 3a, b depict the correlations between the Raman shifts and PL peak, with color-coded data from different regions. In general, there is a strong correlation in peak position between the E$_{2g}^1$ and PL but weaker between the A$_{1g}$ and PL. We also note that typically for the interior region, the PL peak position variation is not as significant as the edge regions. As reported in the literature, with a relatively small stress applied to the film, the shift of Raman and PL peak positions show a linear dependence on the strain [22]. If the strain is the only reason for the inho-

mogeneity, there should be a strong correlation between the Raman and PL peak position maps. The correlation coefficient can be obtained by dividing the covariance of each variation by their standard deviations, and the value always lies between −1 and 1. We calculated the correlation coefficients between the E$_{2g}^1$/A$_{1g}$ and PL peak positions over the whole maps of the triangle, yielding 0.856/0.616, respectively. The correlation coefficient between the E$_{2g}^1$ and A$_{1g}$ peak position is 0.678. Here the correlations between the Raman peak positions and PL peak position are much higher in our WS$_2$ sample than that in the MoS$_2$ samples in the previous study [27].

The correlation coefficients between Raman and PL peak positions, though exhibiting strong correlations, are smaller than 1, also indicating that strain is not the only effect. To have a closer examination of these correlations at the apex, edge and central regions, as labelled in Fig. 1a, the regional correlation coefficients between the peak positions of E$_{2g}^1$ and PL and those of E$_{2g}^1$ and A$_{1g}$ from these regions are calculated individually, shown in Fig. 3c, d. Since A$_{1g}$ and PL peak positions may be impacted by various factors other than strain, we take the shift of E$_{2g}^1$ peak position, which is mostly affected by strain in the WS$_2$ monolayer, as the indicator to represent the strain. As shown in Fig. 3c, the correlation coefficients of the peak positions between E$_{2g}^1$ and PL in A1 and E3 are rather high, 0.83289 and 0.88803,
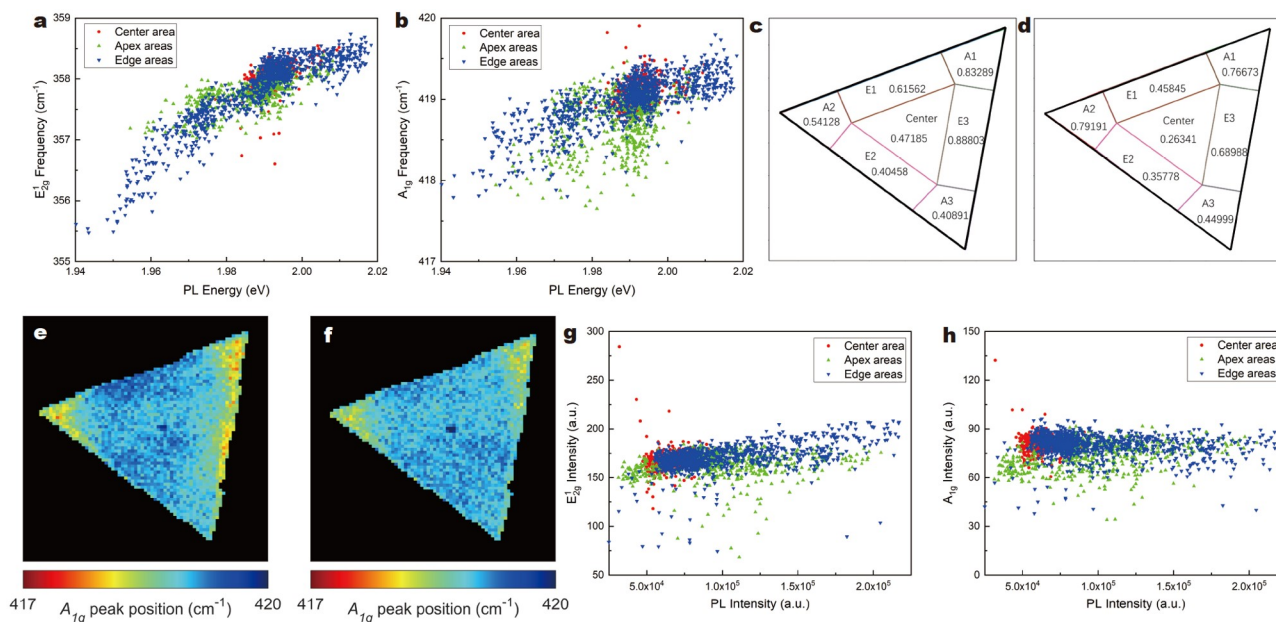
Figure 3 Correlations between Raman and PL. Correlations between (a) E_{2g}^1 and PL peak positions, and (b) A_{1g} and PL peak positions. Regional correlation coefficients between (c) E_{2g}^1 and PL peak positions, and (d) E_{2g}^1 and A_{1g} peak positions at different regions of the monolayer WS_2 triangle. A_{1g} peak position map of the WS_2 triangle (e) before and (f) after subtracting the strain-induced shifts. Correlations between (g) E_{2g}^1 and PL intensities, and (h) A_{1g} and PL intensities.

respectively, while those in other regions only show modest correlations. Thus, the higher coefficients in A1 and E3 regions suggest that the inhomogeneity of the PL peak position map in these two regions are mainly caused by the strain effect. Similarly, the A1 and E3 region, as well as A2, show strong local correlations between the E_{2g}^1 and A_{1g} peak positions in Fig. 3d. In general, the exterior regions have higher correlation coefficients than the central region. Therefore, as a whole, the correlation coefficient between E_{2g}^1 and PL is higher than that between A_{1g} and PL, indicating that A_{1g} is likely more affected by other effects. However, on the regional scale, in selected regions (e.g., A1, A2, and E3) where the strain is the dominant perturbation, E_{2g}^1 and A_{1g} can still be highly correlated.

Doping in the film, which has a minor effect on the shift of the E_{2g}^1 mode, can significantly affect the A_{1g} mode and PL, including the shift of peak position. Due to merging the doping-induced shift of peak position with the strain-induced shift, the correlation between the peak positions of E_{2g}^1 and PL or E_{2g}^1 and A_{1g} is expected to be weakened, because the distribution of the doping concentration in the film is also nonuniform. To further evaluate the doping-induced shift of the A_{1g} peak position quantitatively, the contribution of strain to the shift of the A_{1g} peak position can be subtracted from the A_{1g} mode frequency, by using the strain values that are extracted from the map of the E_{2g}^1 peak position. The original A_{1g} peak position map of the triangle is shown in Fig. 3e, and the new map of the A_{1g} peak position that attributes to doping alone is shown in Fig. 3f. The net doping-related peak positions in the A1 and A2 regions clearly exhibit relative redshifts compared with other regions, indicating that these regions bear different doping situations from other regions.

By inspecting the intensity maps of Fig. 2d–f, the A1 and A2 regions show relatively lower intensity than other regions, consistently for E_{2g}^1, A_{1g} and PL. CVD-grown TMD monolayers

inevitably bear structural defects, such as interfacial defects occurring at the surface of the substrate and/or the lower sulfur layer, mono-sulfur vacancy (V_S), di-sulfur vacancy (V_{S2}), and sulfur adatoms, which are originated from imperfections of the growth process [24]. These sulfur-related defects have been directly observed by scanning transmission electron microscopy (STEM) in monolayer MoS_2 and WS_2 [24,39]. Among all these defects, some are shallow defects that behave like carrier dopants, such as V_S that has been observed to dominate in the CVD-grown films and is an n-type dopant in the TMD monolayer [40]. Besides the shallow defects in the WS_2 layer, the interaction between the substrate and film such as chemical bonding may also give rise to charge transfer, which can significantly tune the doping situation in the film [14]. The reduction of intensity in A1 and A2 can be primarily attributed to the doping effect, which is consistent with the observed redshifts in the A_{1g} and PL peak positions. However, the intensity reduction for E_{2g}^1 in A1 and A2 regions cannot be explained by the doping effect, because doping has negligible impact on the intensity of E_{2g}^1 mode [33,41]. Instead, it could be explained as that the A1 and A2 regions are less strained than the general region based on the E_{2g}^1 peak mapping result (Fig. 2a), and thus, they do not benefit the resonant excitation effect, which will be described below.

Regarding the intensity in the E3 region, both E_{2g}^1 and PL show enhanced intensity. It has been reported that the intensity of Raman modes in WS_2 may be affected by the resonance effect between the excitation laser energy and the X_C state of WS_2 [42], and it is observed that in the epitaxial WS_2 films grown on the sapphire substrate the E_{2g}^1 mode intensity is enhanced with increased tensile strain under 441.6 nm excitation [12]. Therefore, we suggest that the observation of the enhanced intensity of the E_{2g}^1 mode in the E3 region is due to the strain induced resonant excitation effect. The intensity enhancement is also

expected for A_{1g} but to a less extent [42], which is consistent with the weaker enhancement of A_{1g} in the E3 region, as shown in Fig. 2e. As there is relatively more tensile strain in the E3 region, the overall PL peak energies in the E3 region redshift as compared with its surrounding regions, leading to a self-localization effect where the locally excited carriers are trapped at the excitation site instead of partially diffusing away in the general regions [43]. We also note that there is a line in the E_{2g}^1 intensity map, which exhibits lower intensity than the surrounding regions, extending from the center of the triangle to the E3 region. According to the E_{2g}^1 peak position map (Fig. 2a), E3 endures tensile strain different from other regions, and the strain might be strong enough to deform the crystal structure or even introduce a crack, which could significantly decrease the intensity of the E_{2g}^1 mode. This line can also be seen faintly in the A_{1g} intensity map.

Fig. 3g, h plot the correlations between the E_{2g}^1/A_{1g} Raman intensities and PL intensity. The correlation coefficients are much weaker than those of the peak positions. This is understandable because the dominant influencing effects could be rather different for the respective intensities. The E_{2g}^1 intensity is primarily affected by strain through the resonant effect; although both the A_{1g} and PL intensity are sensitive to doping, PL is also very sensitive to the nonradiative defects. Hence the correlations between each other may not be as straightforward as those for their peak positions. However, the calculated correlation coefficients can still qualitatively explain the relationships between the intensities of E_{2g}^1/A_{1g} and PL in different regions. The regional correlation coefficients are shown in Fig. S2. Between the intensities of E_{2g}^1 and PL, among the three edge regions, E3 shows a correlation coefficient of 0.39682, stronger than E1 and E2, which are 0.25584 and −0.13462, respectively. This also explains that strain plays a more dominating role in E3, where the increasing of tensile strain can increase both the intensities of E_{2g}^1 and PL. Between the intensities of A_{1g} and PL, for the apex regions, the A1 and A2 regions show positive correlations, whose correlation coefficients are 0.42394 and 0.49174, respectively, while the A3 region shows a negative correlation with a correlation coefficient of −0.38397. Although showing positive correlations in A1 and A2 as they both are affected by doping, the values are small, because PL is also sensitive to nonradiative defects. As for the negative correlation in A3, doping effect is likely weak, since A_{1g} is fairly uniform in terms of both peak position and intensity; on the other hand, nonradiative centers could potentially deplete the doping and thus, increase the A_{1g} intensity but always lower the PL intensity. The intensities of A_{1g} and PL in the A3 region are both higher than those in the A1 and A2 regions, indicating that the A3 region has less doping. In the central region, both E_{2g}^1 and A_{1g} Raman intensities are fairly uniform, and they are higher than those in the A1 and A2 regions, indicating that the central region has less doping. However, the PL intensities in this region are weaker than most regions, except for A1 and A2. The correlation coefficients between the intensities of E_{2g}^1/A_{1g} and PL are almost zero in this region, implying that neither the strain nor doping effect is the decisive factor of the inhomogeneity of Raman and PL intensity. Rather, the inhomogeneity is caused by other subtle effects, such as nonradiative deep defects.

Interestingly, PL in the regions between central and A1/A2 regions exhibits much higher intensities than in most others. The high intensities in these two regions are different from those

in E3. In E3, the tensile strain shrinks the bandgap so that free excitons are held in this region, thus leading to the increase of the PL intensity. However, in the regions between central and A1/A2 regions, the PL peak positions are somewhat blue-shifted compared with those in E3, so the localization effect, if any, is likely very weak. Thus, one possible explanation to this observation is that these two regions have a better crystal quality than others or bear less nonradiative defects. To gain more insight to the PL intensity variation, we further explicitly examine three representative locations: P1 (in A1), P2 (in C), and P3 (in between A1 and C, showing strong PL), as labelled in Fig. 2f. The corresponding PL spectra are shown in Fig. 2j, and the normalized spectra are shown in Fig. 2k. Compared with P3, both P1 and P2 show much weaker PL intensity. However, P1 exhibits a redshift in the peak energy whereas P2 merely an intensity reduction. We may interpret the intensity reduction at P2 as due to the presence of a large density of non-radiative recombination centers that do not usually affect the Raman signal, as in the case for bulk semiconductors [44]. On the other hand, the changes at P1 could be related to the defect induced doping effect that is known to cause the formation of trions with red-shifted and weakened PL [20]. Also, the Raman spectrum of A_{1g} mode (Fig. S3) from P1 is broader than those from P2 and P3, suggesting that P1 is inhomogeneous in doping. The excitation power dependent PL was carried out at location P1 and P2 (Fig. S4). With increasing excitation density, the lineshape of the normalized PL at P2 remains unchanged while that at P1 clearly shows an increasing weight of X_A- in the PL spectrum, which also indicates the doping effect at P1. Therefore, we can conclude that the non-uniformity in PL intensity can be attributed to the inhomogeneous distribution of defects that either behave as non-radiative centers or contribute to doping.

For the linewidth mapping results shown in Fig. 2g–i, the spatial variations for the Raman modes are smaller than that for PL. The correlations between the Raman linewidths and PL linewidth are shown in Fig. S5. The correlation coefficients between each other turn out to be very small, demonstrating weak or no correlation. Generally speaking, both strain and doping can change the linewidth of Raman and PL. However, both strain and doping may shift the PL peak position, and the former can indirectly through inhomogeneity and the latter can directly affect the PL linewidth. For the E_{2g}^1 mode, shown in Fig. 2g, the most noticeable inhomogeneity, linewidth broadening, occurs in the E3 region with the largest strain deviation as compared with the surrounding regions. For the A_{1g} mode, Fig. 2h, the most linewidth broadening occurs in A1 and A2 regions, which could be due to the inhomogeneity in doping in these two regions. It has been reported that the out-of-plane lattice vibrations can be affected by structural defects (e.g., sulfur vacancy V_S) in monolayer WS_2, similar to the generation mechanism of the D mode in graphene [45]. With V_S in the monolayer WS_2, the D mode may split from the A_{1g} mode with increasing defect density. Therefore, the width of the A_{1g} mode will be broadened by the D mode if there are structural defects in the CVD-grown film. For PL (Fig. 2i), the most apparent linewidth broadening occurs in the A1 and A2 regions associated with doping/defects. Significantly, the regions showing stronger PL, as shown in PL intensity mapping (Fig. 2f), often exhibit smaller linewidths. For instance, the PL linewidth at location P3 is much narrower than that at P1, which is consistent with the suggestion of higher crystallinity of P3. The characteristics of

Table 1 Summary of the characteristics at different regions of the WS$_2$ triangle[a]

Regions	E$_{2g}^1$			A$_{1g}$			PL			Comments
	f	*I*	*w*	*f*	*I*	*w*	*E*	*I*	*w*	
A1	–	↓	–	R	↓	↑	R	↓	↑	More doping and less strain
A2	–	↓	–	R	↓	↑	R	↓	↑	More doping and less strain
A3	–	–	–	–	–	–	–	–	–	Uniform and less nonradiative defects
E1	B	–	–	B	↑	–	B	–	–	Less tensile strain
E2	B	–	–	B	↑	–	B	–	–	Less tensile strain
E3	R	↑	↑	R	–	–	R	↑	↑	More tensile strain
C	–	–	–	–	–	–	–	–	–	Uniform with more nonradiative defects
Line	B	↓	–	B	↓	–	B	–	–	Defective, less tensile strain

a) *f*: frequency; *I*: intensity; *w*: linewidth; *E*: energy; –: no significant change; ↓: decrease; ↑: increase; R: redshift; B: blueshift; line: the crack in the E3 region.
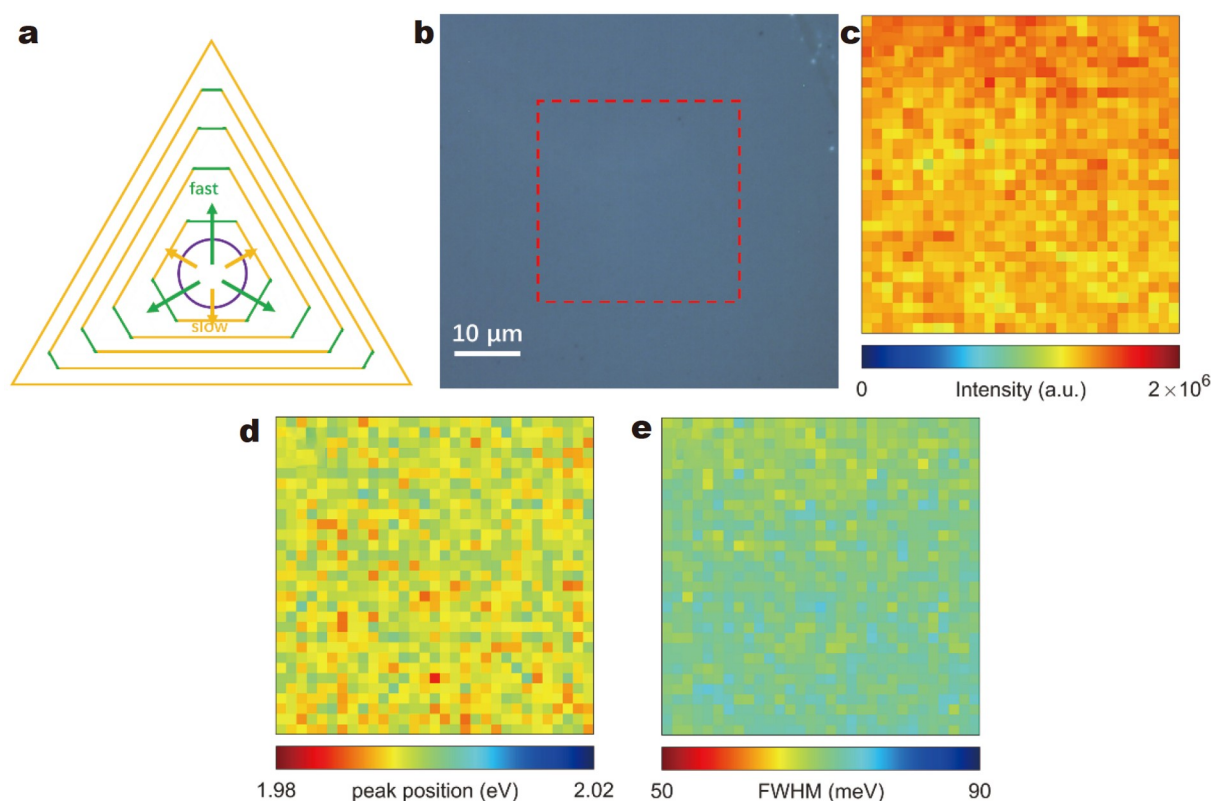
Figure 4 Origin of the strain and doping inhomogeneity. (a) Schematic illustration of the expansion of the monolayer WS$_2$ triangle based on a KWC theory. (b) Optical image of a continuous monolayer WS$_2$ film. The red dash-lined square indicates the mapped region by PL. (c–e) Maps of PL intensity, peak position and FWHM of the continuous WS$_2$ film, respectively. The mapped region is 30 μm × 30 μm.

different regions are summarized in Table 1.

Origins of the inhomogeneity

As noted previously, the non-uniformity of Raman and PL maps originates from the perturbations of local environment during the monolayer growth. The growth process usually starts with the planar nucleation of WS$_2$ nanoparticles, shown as a bright spot at the center of the triangle in the optical image (Fig. 1a), and then expands along all directions to form the monolayer triangle. Though WS$_2$ has a hexagonal crystal structure, most as-

grown WS$_2$ flakes maintain a triangular shape, which is the consequence of a kinetic Wulff construction (KWC) mechanism [46]. As shown in Fig. 4a, the growth rate along the apex direction of the triangle usually is higher than that along the edge direction. Even along the three apex or edge directions, the growth rates may differ from each other. Due to the anisotropic growth rate, the chemical bonding between the monolayer and substrate in the apex regions could be non-uniform across the triangle. Since a fast-cooling process at the final stage of the growth from the growth temperature could create a contraction

mismatch, the non-uniform bonding strength could lead to inhomogeneous strain distribution across the triangle. In our case, for example, the E3 region suffers more contraction force, and hence more tensile strain emerges there. This explains the most redshifts of the E_{2g}^1 mode frequency as well as the PL peak energy in the E3 region. In addition, one should keep in mind that the nonuniformity of the substrate could have a significant impact on the uniformity of the epitaxial film. It is known that the sapphire surface may exhibit different atomic configurations, thus, affecting the initial phase of the epitaxial III-nitride film [47].

It is worth noting that the borderline of the triangle mostly shows strong PL emission, as shown in Fig. 2f. According to the correlation between PL intensity and nonradiative defect density, the WS$_2$ structure at the borderline contains less such defects. In the growth of the monolayer, the atoms at the frontier of the flake always become active sites for WS$_2$ compound to deposit. Therefore, the crystallization quality at the borderline regions tends to be better than other regions [48]. As a result, the defect density in the borderline regions could be lower than the most interior regions (with some exceptions, e.g., P3), leading to a higher PL yield. Continuous WS$_2$ monolayer can be produced when multiple adjacent triangles expand to connect with each other to form a larger region (Fig. 4b, an optical image of a continuous film). We performed PL mapping on such a monolayer film, and the PL intensity, peak position and FWHM maps are shown in Fig. 4c–e, respectively. As can be seen in the maps, the variations of intensity, peak position and FWHM in the continuous film are much smaller than those in the triangles. With a longer growth time, the chemical bonding between the WS$_2$ film and substrate is getting more uniform as well as the WS$_2$ stoichiometry across the film. Thus, the distributions of strain and doping concentration in the film becomes more homogeneous, i.e., less variations in spectroscopic mapping. Interestingly, the overall magnitude of the epitaxial strain is reduced, manifesting as overall blueshift of the PL peak compared with the triangular sample [12].

CONCLUSIONS

In summary, we have used μ-Raman/PL mapping to study the inhomogeneity of strain, doping and defects in the CVD-grown epitaxial WS$_2$ monolayers by analyzing the peak position, intensity and FWHM of Raman and PL spectra, and the correlations between these properties. We have observed non-uniform strain in the as-grown WS$_2$ triangle and proposed that the strain originates from the fast-cooling process at the final stage of CVD growth. The maximum strain difference within the triangle can be extracted and quantified statistically from the peak position maps of the E_{2g}^1 Raman mode and PL. Also, by correlating the maps of PL and A$_{1g}$ mode, we are able to examine the doping and non-radiative defect inhomogeneity in the WS$_2$ triangle. Our results provide a practical way to investigate the inhomogeneity of CVD-grown two-dimensional materials and insights to improve the growth process to achieve a better material quality. We have found that although a strong numerical correlation in the variations of two spectroscopy quantities often indicates a common underlying mechanism, it is not always the case when other multiple quantities are simultaneously analyzed, even within the same sample. This study indicates the importance of understanding the interplay of multiple physical mechanisms that may manifest rather differently in different regions of one sample, not to mention in samples prepared differently.

1 Fu Q, Han J, Wang X, *et al.* 2D transition metal dichalcogenides: Design, modulation, and challenges in electrocatalysis. Adv Mater, 2021, 33: 1907818

2 Chen B, Chao D, Liu E, *et al.* Transition metal dichalcogenides for alkali metal ion batteries: Engineering strategies at the atomic level. Energy Environ Sci, 2020, 13: 1096–1131

3 Liang Q, Zhang Q, Zhao X, *et al.* Defect engineering of two-dimensional transition-metal dichalcogenides: Applications, challenges, and opportunities. ACS Nano, 2021, 15: 2165–2181

4 Partoens B, Peeters FM. From graphene to graphite: Electronic structure around the K point. Phys Rev B, 2006, 74: 075404

5 Wang C, Yang F, Gao Y. The highly-efficient light-emitting diodes based on transition metal dichalcogenides: From architecture to performance. Nanoscale Adv, 2020, 2: 4323–4340

6 Phan NAN, Noh H, Kim J, *et al.* Enhanced performance of WS$_2$ field-effect transistor through mono and bilayer h-BN tunneling contacts. Small, 2022, 18: 2105753

7 Pei Y, Chen R, Xu H, *et al.* Recent progress about 2D metal dichalcogenides: Synthesis and application in photodetectors. Nano Res, 2021, 14: 1819–1839

8 Ozdemir B, Barone V. Thickness dependence of solar cell efficiency in transition metal dichalcogenides MX$_2$ (M: Mo, W; X: S, Se, Te). Sol Energy Mater Sol Cells, 2020, 212: 110557

9 Zhang Q, Mei L, Cao X, *et al.* Intercalation and exfoliation chemistries of transition metal dichalcogenides. J Mater Chem A, 2020, 8: 15417–15444

10 Yu Y, Li C, Liu Y, *et al.* Controlled scalable synthesis of uniform, high-quality monolayer and few-layer MoS$_2$ films. Sci Rep, 2013, 3: 1866

11 Su L, Zhang Y, Yu Y, *et al.* Dependence of coupling of quasi 2-D MoS$_2$ with substrates on substrate types, probed by temperature dependent Raman scattering. Nanoscale, 2014, 6: 4920–4927

12 Su L, Yu Y, Cao L, *et al.* Effects of substrate type and material-substrate bonding on high-temperature behavior of monolayer WS$_2$. Nano Res, 2015, 8: 2686–2697

13 Buscema M, Steele GA, van der Zant HSJ, *et al.* The effect of the substrate on the Raman and photoluminescence emission of single-layer MoS$_2$. Nano Res, 2014, 7: 561–571

14 Yu Y, Yu Y, Xu C, *et al.* Engineering substrate interactions for high luminescence efficiency of transition-metal dichalcogenide monolayers. Adv Funct Mater, 2016, 26: 4733–4739

15 Su L, Yu Y, Cao L, *et al. In situ* monitoring of the thermal-annealing effect in a monolayer of MoS$_2$. Phys Rev Appl, 2017, 7: 034009

16 Tang L, Tan J, Nong H, *et al.* Chemical vapor deposition growth of two-dimensional compound materials: Controllability, material quality, and growth mechanism. Acc Mater Res, 2021, 2: 36–47

17 Qin Z, Loh L, Wang J, *et al.* Growth of Nb-doped monolayer WS$_2$ by liquid-phase precursor mixing. ACS Nano, 2019, 13: 10768–10775

18 Zhang P, Cheng N, Li M, *et al.* Transition-metal substitution-induced lattice strain and electrical polarity reversal in monolayer WS$_2$. ACS Appl Mater Interfaces, 2020, 12: 18650–18659

19 Gutiérrez HR, Perea-López N, Elías AL, *et al.* Extraordinary room-temperature photoluminescence in triangular WS$_2$ monolayers. Nano Lett, 2013, 13: 3447–3454

20 Shang J, Shen X, Cong C, *et al.* Observation of excitonic fine structure in a 2D transition-metal dichalcogenide semiconductor. ACS Nano, 2015, 9: 647–655

21 Wang XH, Ning JQ, Su ZC, *et al.* Photoinduced doping and photoluminescence signature in an exfoliated WS$_2$ monolayer semiconductor. RSC Adv, 2016, 6: 27677–27681

22 Wang Y, Cong C, Yang W, *et al.* Strain-induced direct–indirect bandgap transition and phonon modulation in monolayer WS$_2$. Nano Res, 2015, 8: 2562–2572

23 Tongay S, Suh J, Ataca C, *et al.* Defects activated photoluminescence in

two-dimensional semiconductors: Interplay between bound, charged and free excitons. Sci Rep, 2013, 3: 2657

24 Zhou W, Zou X, Najmaei S, et al. Intrinsic structural defects in monolayer molybdenum disulfide. Nano Lett, 2013, 13: 2615–2622

25 Kim JY, Gelczuk Ł, Polak MP, et al. Experimental and theoretical studies of native deep-level defects in transition metal dichalcogenides. npj 2D Mater Appl, 2022, 6: 75

26 Liu Z, Amani M, Najmaei S, et al. Strain and structure heterogeneity in MoS$_2$ atomic layers grown by chemical vapour deposition. Nat Commun, 2014, 5: 5246

27 Lu AY, Martins LGP, Shen PC, et al. Unraveling the correlation between Raman and photoluminescence in monolayer MoS$_2$ through machine-learning models. Adv Mater, 2022, 34: 2202911

28 Yu Y, Hu S, Su L, et al. Equally efficient interlayer exciton relaxation and improved absorption in epitaxial and nonepitaxial MoS$_2$/WS$_2$ heterostructures. Nano Lett, 2015, 15: 486–491

29 Kotsakidis JC, Zhang Q, Vazquez de Parga AL, et al. Oxidation of monolayer WS$_2$ in ambient is a photoinduced process. Nano Lett, 2019, 19: 5205–5215

30 Berkdemir A, Gutiérrez HR, Botello-Méndez AR, et al. Identification of individual and few layers of WS$_2$ using Raman spectroscopy. Sci Rep, 2013, 3: 1755

31 Zhu B, Chen X, Cui X. Exciton binding energy of monolayer WS$_2$. Sci Rep, 2015, 5: 9218

32 Dadgar AM, Scullion D, Kang K, et al. Strain engineering and Raman spectroscopy of monolayer transition metal dichalcogenides. Chem Mater, 2018, 30: 5148–5155

33 Chakraborty B, Bera A, Muthu DVS, et al. Symmetry-dependent phonon renormalization in monolayer MoS$_2$ transistor. Phys Rev B, 2012, 85: 161403

34 Rathod UP, Egede J, Voevodin AA, et al. Extrinsic p-type doping of few layered WS$_2$ films with niobium by pulsed laser deposition. Appl Phys Lett, 2018, 113: 062106

35 Wang F, Li S, Bissett MA, et al. Strain engineering in monolayer WS$_2$ and WS$_2$ nanocomposites. 2D Mater, 2020, 7: 045022

36 Peimyoo N, Yang W, Shang J, et al. Chemically driven tunable light emission of charged and neutral excitons in monolayer WS$_2$. ACS Nano, 2014, 8: 11320–11329

37 Yim WM, Paff RJ. Thermal expansion of AlN, sapphire, and silicon. J Appl Phys, 1974, 45: 1456–1457

38 Zobeiri H, Xu S, Yue Y, et al. Effect of temperature on Raman intensity of nm-thick WS$_2$: Combined effects of resonance Raman, optical properties, and interface optical interference. Nanoscale, 2020, 12: 6064–6078

39 Wang S, Robertson A, Warner JH. Atomic structure of defects and dopants in 2D layered transition metal dichalcogenides. Chem Soc Rev, 2018, 47: 6764–6794

40 Zhang F, Lu Y, Schulman DS, et al. Carbon doping of WS$_2$ monolayers: Bandgap reduction and p-type doping transport. Sci Adv, 2019, 5: eaav5003

41 Iqbal MW, Shahzad K, Hussain G, et al. Gate dependent phonon shift in tungsten disulfide (WS$_2$) field effect transistor. Mater Res Express, 2019, 6: 115909

42 del Corro E, Botello-Méndez A, Gillet Y, et al. Atypical exciton–phonon interactions in WS$_2$ and WSe$_2$ monolayers revealed by resonance Raman spectroscopy. Nano Lett, 2016, 16: 2363–2368

43 Feng J, Qian X, Huang CW, et al. Strain-engineered artificial atom as a broad-spectrum solar energy funnel. Nat Photon, 2012, 6: 866–872

44 Chen Q, McKeon BS, Zhang SY, et al. Impact of individual structural defects in GaAs solar cells: A correlative and in operando investigation of signatures, structures, and effects. Adv Opt Mater, 2021, 9: 2001487

45 Lee C, Jeong BG, Yun SJ, et al. Unveiling defect-related Raman mode of monolayer WS$_2$ via tip-enhanced resonance Raman scattering. ACS Nano, 2018, 12: 9982–9990

46 Shu H, Chen X, Ding F. The edge termination controlled kinetics in graphene chemical vapor deposition growth. Chem Sci, 2014, 5: 4639–4645

47 Liu Z, Liu B, Ren F, et al. Atomic-scale mechanism of spontaneous polarity inversion in AlN on nonpolar sapphire substrate grown by MOCVD. Small, 2022, 18: 2200057

48 Duan X, Wang C, Pan A, et al. Two-dimensional transition metal dichalcogenides as atomically thin semiconductors: Opportunities and challenges. Chem Soc Rev, 2015, 44: 8859–8876

Author contributions   Zhang Y conceived the idea and supervised this work. Yu Y and Cao L performed the CVD-growth of the samples. Su L conducted the experiments and analyzed the data. Su L and Zhang Y wrote the paper with support from Yu Y and Cao L. All authors contributed to the general discussion.

Conflict of interest   The authors declare that they have no conflict of interest.

Supplementary information   Supporting data are available in the online version of the paper.

Liqin Su is an assistant professor at the College of Optical and Electronic Technology, China Jiliang University. He received his PhD degree in 2015 from the University of North Carolina at Charlotte. His research interests focus on two-dimensional materials and optical spectroscopy.

Yong Zhang is a Bissell Distinguished Professor at the Electrical and Computer Engineering Department, UNC-Charlotte. He received his BS and MS degrees from Xiamen University and PhD degree from Dartmouth College. He was a postdoc and later a Senior Scientist at the National Renewable Energy Laboratory. His research interests include electronic and optical properties of semiconductors, organic-inorganic hybrid materials, impurity and defects in semiconductors, and novel materials and device architectures for applications in optoelectronics, energy, and electronic-photonic integrated circuits.

光谱特征关联性分析用于研究CVD生长的单层二硫化钨非均匀性机制

苏立钦[1,2], 余一飞[3], 曹林友[3], 张勇[2*]

摘要   化学气相沉积(CVD)已被证明是生产二维材料(包括二硫化钨(WS$_2$))最有效的方法. 然而, CVD生长的WS$_2$单层中存在的应变、掺杂和缺陷的不均匀性会显著影响材料的光学和电子特性, 从而影响其器件应用. 在本研究中, 我们通过CVD方法在蓝宝石衬底上生长了介观尺寸的三角形单层WS$_2$, 并利用空间分辨的显微拉曼和光致发光(PL)光谱技术系统地表征了单层WS$_2$中的应变、掺杂和非辐射缺陷中心的不均匀性. 我们从全域(整个单层WS$_2$三角形)和分区域(如顶点、边缘、中心)两个维度对其拉曼和PL光谱的相关参数(即峰值位置、强度和半峰宽)随位置的变化进行了相关性分析, 发现单层WS$_2$三角形的不同区域往往表现出明显不同的应变、掺杂和缺陷状态. 这项研究揭示并解释了单层WS$_2$应变、掺杂和缺陷的不均匀性. 此外, 我们发现当介观尺寸的三角形结构扩展到连续薄膜时, 不均匀性大大降低. 我们的工作表明, 对光谱特征的相关性分析并辅以对物理机制的了解有助于全面理解材料生长带来的不均匀性, 并为优化二维材料的生长过程和器件加工提供指导.